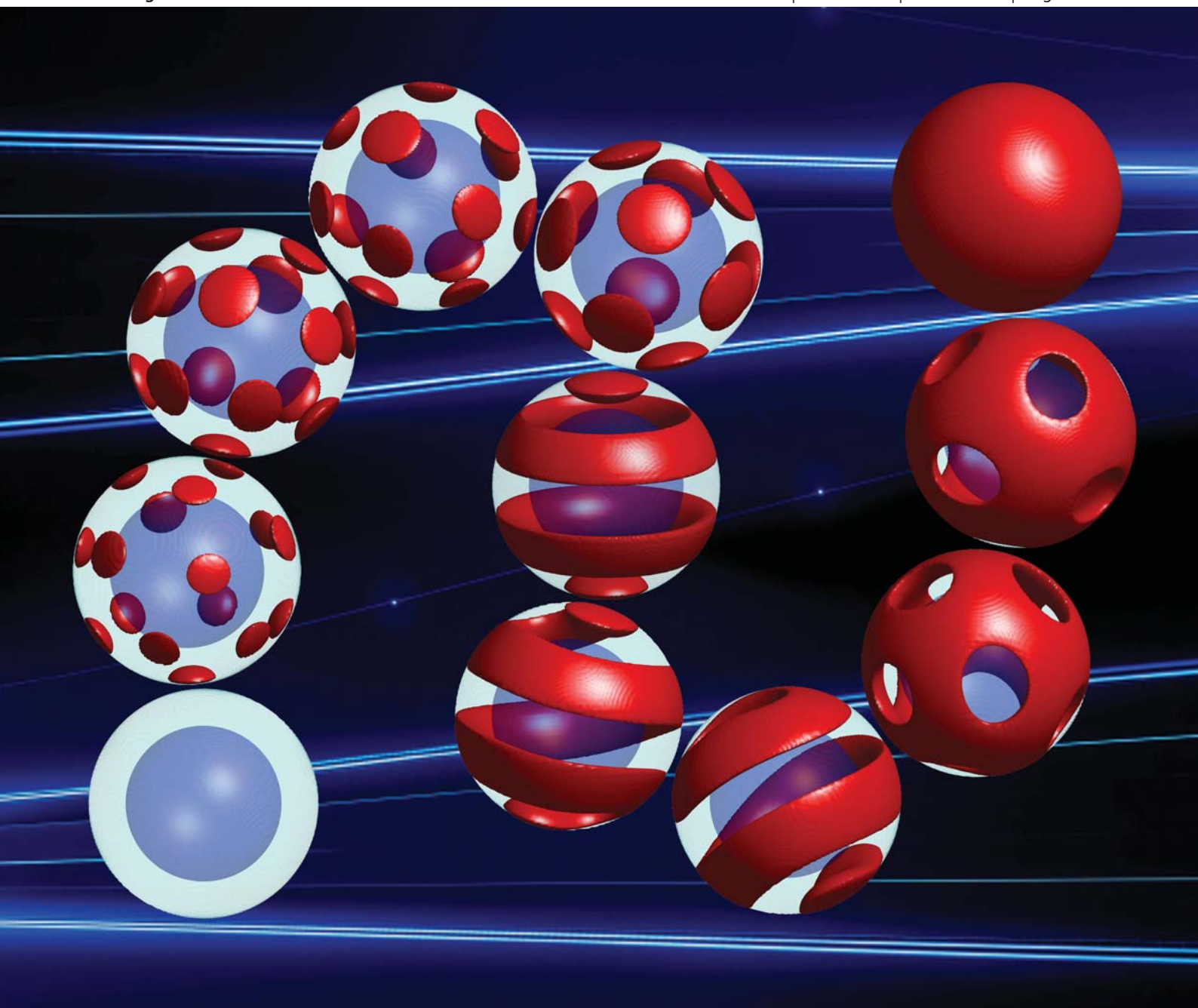


Soft Matter

www.rsc.org/softmatter

Volume 7 | Number 11 | 7 June 2011 | Pages 5049–5452



ISSN 1744-683X

RSC Publishing

PAPER

Mark W. Matsen *et al.*
Self-consistent field theory for diblock
copolymers grafted to a sphere



International Year of
CHEMISTRY
2011



1744-683X(2011)7:11;1-M

Cite this: *Soft Matter*, 2011, **7**, 5128

www.rsc.org/softmatter

PAPER

Self-consistent field theory for diblock copolymers grafted to a sphere

Bart Vorselaars,^{*a} Jaeup U. Kim,^b Tanya L. Chantawansri,^{†c} Glenn H. Fredrickson^c and Mark W. Matsen^{*a}

Received 2nd November 2010, Accepted 12th January 2011

DOI: 10.1039/c0sm01242d

An efficient numerical self-consistent field theory (SCFT) algorithm is developed for treating structured polymers on spherical surfaces. The method solves the diffusion equations of SCFT with a pseudo-spectral approach that combines a spherical-harmonics expansion for the angular coordinates with a modified real-space Crank–Nicolson method for the radial direction. The self-consistent field equations are solved with Anderson-mixing iterations using dynamical parameters and an alignment procedure to prevent angular drift of the solution. A demonstration of the algorithm is provided for thin films of diblock copolymer grafted to the surface of a spherical core, in which the sequence of equilibrium morphologies is predicted as a function of diblock composition. The study reveals an array of interesting behaviors as the block copolymer pattern is forced to adapt to the finite surface area of the sphere.

1. Introduction

The self-assembly of thin diblock-copolymer films has received considerable attention over the last 20 years as an efficient means of patterning surfaces on the nanometre scale for such applications as the construction of high-capacity data storage devices, waveguides, quantum dot arrays, dielectric mirrors, nanoporous membranes, and nanowires.¹ More recently, researchers have begun exploring the advantages of grafting polymers to a substrate, either as end-tethered diblocks^{2–4} or as binary mixtures of chemically distinct homopolymers.^{5–8} Among the advantages is that grafted films are more robust and able to survive harsher conditions, making it possible to design responsive films where the morphology adapts to changes in the environment.⁹ These films can also be grafted to spherical nanoparticles,¹⁰ creating colloids with environmentally-responsive surface patterns. So far, these attempts have focused on binary brushes,^{11–16} but efforts are now underway to graft particles with diblock copolymers as depicted in Fig. 1.¹⁷

A solid theoretical understanding of these grafted films will be essential if we are to take full advantage of their potential applications. A straightforward approach to modeling their behavior is to perform molecular dynamics¹⁸ or Monte Carlo¹⁹ simulations, but the computational demands limit such studies to either short chains or low grafting densities. A far cheaper

approach is to use simple phenomenological models based on Landau–Ginzburg free energy functionals,^{20,21} but unfortunately these theories have difficulty in accounting for the microscopic details of the film. For example, they would struggle to distinguish between a diblock copolymer brush and a mixed binary brush. An intermediate strategy is to use self-consistent field theory (SCFT), which is based on a well-established coarse-grained microscopic model. There have already been SCFT calculations²² in one dimension for morphologies with no angular dependence and in two dimensions for morphologies with either rotational symmetry²³ or without any radial dependence.^{24–26} The challenge, however, is to perform full 3D calculations. Roan^{27,28} has managed this, but he reports that his algorithm is computationally demanding, potentially taking years of CPU time to generate a self-consistent solution.

Here we devise an efficient SCFT algorithm for studying structured 3D polymeric films on spherical substrates. Rather than following the real-space approach of Roan,^{27,28} we extend the pseudo-spectral approach²⁹ developed earlier by Chantawansri *et al.*²⁵ for the special case of 2D morphologies without any radial (*i.e.*, r) dependence. To solve the diffusion equation in SCFT, Chantawansri *et al.* used operator splitting combined with transforms between a real-space mesh in spherical-polar coordinates, $\theta = j\pi/(n_\theta - 1)$ for $j = 0, 1, \dots, n_\theta - 1$ and $\varphi = 2k\pi/n_\varphi$

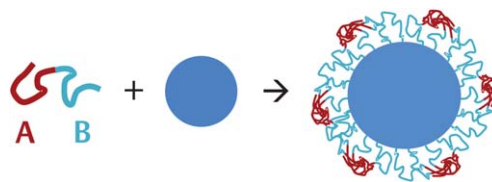


Fig. 1 A melt of diblock copolymers grafted to a spherical core, creating a chemically-patterned nanoparticle.

^aSchool of Mathematical and Physical Sciences, University of Reading, Whiteknights, Reading, RG6 6AX, UK. E-mail: b.vorselaars@reading.ac.uk; m.w.matsen@reading.ac.uk

^bSchool of Mechanical and Advanced Materials Engineering, UNIST, Korea

^cDepartments of Chemical Engineering and Materials, University of California, Santa Barbara, California, USA

[†]Current address: Army Research Laboratory, Aberdeen Proving Grounds, Maryland, USA.

for $k = 0, 1, \dots, n_\varphi - 1$, where the field part of the operator is applied, and an expansion in spherical harmonics, $Y_{\ell m}(\theta, \varphi)$, where the Laplacian part of the operator is dealt with. To incorporate an r dependence requires an additional operation for the radial part of the Laplacian, for which we develop a modified Crank–Nicolson method. We also improve the iteration scheme for adjusting the fields self-consistently by employing Anderson mixing³⁰ with an adaptive mixing parameter and a varying number of histories. The convergence is further aided by an alignment procedure that counters rotational drift in the fields.

We apply the algorithm to a simple system of AB diblock copolymers grafted to a spherical core by their B ends (Fig. 1). After establishing the numerical accuracy and computational efficiency of the algorithm, we investigate the morphologies and phase transitions produced by varying the composition of the diblock. Just as for flat brushes,⁴ the A-rich domains on the outer surface of the brush evolve from discrete dots to stripes to a layer with holes and finally to a uniform shell. However, this is complicated by the requirement that the resulting patterns must fit within a finite surface area, which produces interesting behavior in much the same way as when block copolymers are confined to cylindrical^{31–35} or spherical^{36–38} cavities. In our case, the packing frustration experienced by the dot/hole patterns is reminiscent of the standard Tammes^{39,40} and Thomson^{39,41} problems of positioning disks and charged particles, respectively, on a sphere.

2. Theory and numerical method

This section introduces the self-consistent field theory (SCFT)^{42–44} and our numerical algorithm for solving it. They are described for a melt of n_c AB diblock-copolymer chains uniformly grafted by their B ends to a spherical core of radius R_c (Fig. 1). Each diblock molecule consists of N segments, of which a fraction f forms the A block, and has a natural end-to-end length of $R_0 = aN^{1/2}$. The incompatibility of the A and B segments is controlled by the usual Flory–Huggins χ parameter. For simplicity, we assume that the polymer/air surface tensions, $\gamma_{A/\text{air}}$ and $\gamma_{B/\text{air}}$, are sufficiently large (relative to the A/B interfacial tension, $\gamma_{A/B}$) that the copolymer film forms a shell of uniform thickness L . Furthermore, the outer air surface is assumed to be neutral (*i.e.*, $\gamma_{A/\text{air}} = \gamma_{B/\text{air}}$), although it would be straightforward to include a surface affinity.⁴ Similarly, the core is also taken to be neutral.

2.1. Self-consistent field theory

The SCFT for a diblock-copolymer brush on a flat surface has been introduced earlier,⁴ and therefore we simply summarize the relevant equations. As before, the A and B segments are subjected to fields,

$$w_A(\mathbf{r}) = \chi N \phi_B(\mathbf{r}) + \xi(\mathbf{r}) \quad (1)$$

$$w_B(\mathbf{r}) = \chi N \phi_A(\mathbf{r}) + \xi(\mathbf{r}) \quad (2)$$

which are self-consistently related to the dimensionless A- and B-segment concentrations,

$$\phi_A(\mathbf{r}) = \int_0^f q(\mathbf{r}, s) q^\dagger(\mathbf{r}, s) ds \quad (3)$$

$$\phi_B(\mathbf{r}) = \int_f^1 q(\mathbf{r}, s) q^\dagger(\mathbf{r}, s) ds \quad (4)$$

respectively. The pressure field, $\xi(\mathbf{r})$, acts to enforce the incompressibility condition,

$$\phi_A(\mathbf{r}) + \phi_B(\mathbf{r}) = 1 \quad (5)$$

One of the computationally demanding parts of SCFT is the evaluation of the partial partition functions, $q(\mathbf{r}, s)$ and $q^\dagger(\mathbf{r}, s)$, required to evaluate the concentrations. The first of these satisfies the modified diffusion equation,

$$\frac{\partial}{\partial s} q(\mathbf{r}, s) = \left(\frac{R_0^2}{6} \nabla^2 - w_\kappa(\mathbf{r}) \right) q(\mathbf{r}, s) \quad (6)$$

where $\kappa = A$ for $s < f$ and $\kappa = B$ for $s > f$. The second, $q^\dagger(\mathbf{r}, s)$, satisfies the same diffusion equation but with one side multiplied by -1 . Both partition functions are solved subject to homogeneous Neumann boundary conditions^{44,45} at $r = R_c$ and $r = R_c + L$, combined with the initial conditions,^{8,44,46}

$$q(\mathbf{r}, 0) = 1 \quad (7)$$

$$q^\dagger(\mathbf{r}, 1) = \frac{V \delta(r - R_c^+)}{A q(\mathbf{r}, 1)} \quad (8)$$

where $V = 4\pi((R_c + L)^3 - R_c^3)/3$ is the volume occupied by the brush and $A = 4\pi R_c^2$ is the surface area of the core. (eqn (8) ensures that the grafting density, which is proportional to $q(\mathbf{r}, 1)q^\dagger(\mathbf{r}, 1)$, remains uniform.⁴)

The other computationally demanding part of SCFT is adjusting the fields to satisfy eqn (1), (2) and (5). Once this is done, the free energy of the brush, F , is evaluated as

$$\begin{aligned} \frac{F}{n_c k_B T} = & -\frac{1}{A} \int \delta(r - R_c^+) \ln q(\mathbf{r}, 1) d\mathbf{r} \\ & + \frac{1}{V} \int \{ \chi N \phi_A(\mathbf{r}) \phi_B(\mathbf{r}) - w_A(\mathbf{r}) \phi_A(\mathbf{r}) \\ & - w_B(\mathbf{r}) \phi_B(\mathbf{r}) \} d\mathbf{r} \end{aligned} \quad (9)$$

2.2. Modified diffusion equation

Here we solve the modified diffusion eqn (6) with the pseudo-spectral method,^{29,47} used earlier²⁵ for morphologies without any radial dependence. This method involves switching back and forth between real-space and spectral representations. In real space, spatial functions, $f(\mathbf{r})$, are represented on a uniform mesh in spherical-polar coordinates, $\mathbf{r} = (r, \theta, \varphi) = (R_c + i\Delta r, j\Delta\theta, k\Delta\varphi)$, where i, j and k are integers. The mesh spacings are $\Delta r = L/(n_r - 1)$, $\Delta\theta = \pi/(n_\theta - 1)$ and $\Delta\varphi = 2\pi/n_\varphi$, where n_r , n_θ and n_φ are the number of mesh points in the respective directions. Every mesh point, (i, j, k) , corresponds to a cell of volume, ΔV , defined by the intervals, $r \pm \Delta r/2$, $\theta \pm \Delta\theta/2$, and $\varphi \pm \Delta\varphi/2$, apart from the cells at the edge of the mesh.⁴⁸ (Spatial integrals then become discrete sums over the mesh points weighted by their respective ΔV .) The spectral representation,

$$f(r, \theta, \varphi) = \sum_{\ell, m} f_{\ell m}(r) Y_{\ell m}(\theta, \varphi) \quad (10)$$

extends over all the real-valued spherical harmonics, $Y_{\ell m}(\theta, \varphi)$,⁴⁹ up to $\ell \leq \ell_{\max} = n_\theta - 1$. The transformation between these two representations is carried out with the SPHEREPACK 3.2 software package.^{25,50,51}

The pseudo-spectral approach begins with the formal solution of eqn (6),⁵²

$$q(\mathbf{r}, s + \Delta s) = \exp\left(\Delta s \left(\frac{R_0^2}{6} \nabla^2 - w_\kappa(\mathbf{r})\right)\right) q(\mathbf{r}, s) \quad (11)$$

where $\Delta s = 1/(n_s - 1)$ is the grid spacing along the chain contour. (Note that the composition of the diblock, f , is restricted to integer multiples of Δs .) We then split the operator,⁵³ applying one part at a time in the sequence,

$$q^a(r, \theta, \varphi) \equiv \exp\left(-\frac{\Delta s}{2} w_\kappa(\mathbf{r})\right) q(\mathbf{r}, s) \quad (12)$$

$$q_{\ell m}^b(r) \equiv \exp\left(\frac{\Delta s R_0^2}{12} \nabla_{\theta\varphi}^2\right) q_{\ell m}^a(r) \quad (13)$$

$$q_{\ell m}^c(r) \equiv \exp\left(\frac{\Delta s R_0^2}{6} \nabla_r^2\right) q_{\ell m}^b(r) \quad (14)$$

$$q_{\ell m}^d(r) \equiv \exp\left(\frac{\Delta s R_0^2}{12} \nabla_{\theta\varphi}^2\right) q_{\ell m}^c(r) \quad (15)$$

$$q(\mathbf{r}, s + \Delta s) \approx \exp\left(-\frac{\Delta s}{2} w_\kappa(\mathbf{r})\right) q^d(r, \theta, \varphi) \quad (16)$$

Some inaccuracy is introduced by the fact that the different portions of the operator do not commute, but the Strang procedure^{54,55} of splitting the operator into five parts, so as to maintain the invariance under reversal in s , limits the inaccuracy in $q(\mathbf{r}, s)$ to second order in Δs .

In the real-space representation, eqn (12) and (16) correspond to simple multiplications. Since $Y_{\ell m}(\theta, \varphi)$ is an eigenfunction of the angular-part of the Laplacian operator, in the spectral representation, we can replace $\nabla_{\theta\varphi}^2$ by the corresponding eigenvalue, $-\ell(\ell + 1)/r^2$. With this, eqn (13) and (15) also reduce to simple multiplications.

For eqn (14) involving the radial part of the Laplacian, ∇_r^2 , we use a real-space representation for the r coordinate as opposed to transforming to spherical Bessel functions. This is largely because of the delta functions that occur in the fields due to the grafting (and also surface fields had they been included) are not well represented by spectral expansions.⁴ Furthermore, the transformations between real space and spherical Bessel functions are not so straightforward. Admittedly, we could transform ∇_r^2 to Cartesian coordinates by expressing the diffusion equation in terms of $q(\mathbf{r}, s)/r$,⁵⁶ which allows for a simple sine/cosine expansion, but this leads to less convenient Robin boundary conditions.

In real space, we can simply implement the (semi-implicit) Crank–Nicolson approximation,⁵⁷

$$\frac{q_{\ell m}^c(r) - q_{\ell m}^b(r)}{\Delta s} \approx \frac{R_0^2}{6} \nabla_r^2 \left[\frac{q_{\ell m}^c(r) + q_{\ell m}^b(r)}{2} \right] \quad (17)$$

which also maintains the reversal symmetry in s and the second-order accuracy in Δs . The approximation does, however, lead to spurious oscillations in $q^i(\mathbf{r}, s)$ as a result of the discontinuity in its initial condition, eqn (8),⁵⁸ but there is no significant affect on any quantities of interest provided that Δs is sufficiently small relative to Δr .

For Cartesian coordinates in 1D, the Crank–Nicolson algorithm has the advantage that it conserves material [i.e., $V^{-1} \int (\phi_A(\mathbf{r}) + \phi_B(\mathbf{r})) d\mathbf{r} = 1$] to within the floating-point precision of the calculation,⁵⁹ but this property is lost for curved geometries if we represent the Laplacian by simple finite differences. Fortunately, the conservation of material is partially restored (completely restored when there is no angular dependence) if we evaluate $\nabla_r^2 q_{\ell m}(r)$ using a finite-volume technique, where it is viewed as the divergence of a current.⁵⁴ The divergence theorem then transforms the integral of $\nabla_r^2 q_{\ell m}(r)$ over the volume of each cell, ΔV , into a flux through the area of its inner and outer surface elements, $\Delta A_\pm \propto (r \pm \Delta r/2)^2$. This leads to the approximation,

$$\begin{aligned} \nabla_r^2 q_{\ell m}(r) \approx & C_+ [q_{\ell m}(r + \Delta r) - q_{\ell m}(r)] \\ & - C_- [q_{\ell m}(r) - q_{\ell m}(r - \Delta r)] \end{aligned} \quad (18)$$

with $C_\pm = \Delta A_\pm / (\Delta r \Delta V)$, which is accurate to second order in Δr .⁶⁰ Due to the boundary conditions, the fluxes at the extremities of the brush are zero, which are satisfied by setting $C_- = 0$ for $r = R_c$ and $C_+ = 0$ for $r = R_c + L$.

2.3. Iteration scheme

We satisfy the self-consistent field equations iteratively using the Anderson-mixing method employed by Thompson *et al.*³⁰ Before starting, the initial fields, $w_\kappa^{(0)}(\mathbf{r})$, are filtered by transforming to $w_{\kappa, \ell m}^{(0)}(r)$ and back. This is done because the SPHEREPACK subroutines use a different number of points for the real-space mesh than functions for the spherical-harmonic expansion, and thus the transformation is not one-to-one. The iteration procedure is such that the subsequent fields, $w_\kappa^{(n)}(\mathbf{r})$, remain in the space spanned by the spherical harmonics.

The $(n + 1)$ -th iteration begins by calculating the concentrations, $\phi_\kappa^{(n)}(\mathbf{r})$, from the current fields, $w_\kappa^{(n)}(\mathbf{r})$, with which we evaluate the new fields,

$$\tilde{w}_A^{(n)} = \chi N \phi_B^{(n)} + \frac{1}{2} (w_A^{(n)} + w_B^{(n)}) \quad (19)$$

$$\tilde{w}_B^{(n)} = \chi N \phi_A^{(n)} + \frac{1}{2} (w_A^{(n)} + w_B^{(n)}) \quad (20)$$

Note that the fields are always adjusted by an additive constant so that their spatial average is zero.⁴⁴ Next we evaluate the differences,

$$\Delta w_\kappa^{(n)} = \tilde{w}_\kappa^{(n)} - w_\kappa^{(n)} \quad (21)$$

for $\kappa = A$ and B , from which we define

$$\text{err}_n = \frac{1}{\chi N} \left(\frac{1}{V} \sum_{\kappa} \int \left| \Delta w_{\kappa}^{(n)}(\mathbf{r}) \right|^2 d\mathbf{r} \right)^{1/2} \quad (22)$$

as a measure of the numerical inaccuracy in the field conditions. Note that the relative spatial variation in the total polymer concentration, $\phi_A^{(n)}(\mathbf{r}) + \phi_B^{(n)}(\mathbf{r})$, will necessarily be of similar magnitude.

If $\text{err}_n > 10^{-6}$, then we evaluate the improved estimate,^{61,62}

$$w_{\kappa}^{(n+1)} = W_{\kappa}^{(n)} + \lambda \Delta W_{\kappa}^{(n)} \quad (23)$$

where λ is a mixing parameter, and

$$W_{\kappa}^{(n)} = w_{\kappa}^{(n)} + \sum_{m=1}^{n_h} C_m (w_{\kappa}^{(n-m)} - w_{\kappa}^{(n)}) \quad (24)$$

$$\Delta W_{\kappa}^{(n)} = \Delta w_{\kappa}^{(n)} + \sum_{m=1}^{n_h} C_m (\Delta w_{\kappa}^{(n-m)} - \Delta w_{\kappa}^{(n)}) \quad (25)$$

combine a specified number, n_h , of histories. The weightings are given by $C_m = \sum_l (U^{-1})_{ml} V_l$, where $U_{lm} = d_{lm} + d_{00} - d_{0l} - d_{0m}$ and $V_l = d_{00} - d_{0l}$ are evaluated in terms of

$$d_{lm} = \frac{1}{V} \sum_{\kappa} \int \Delta w_{\kappa}^{(n-l)}(\mathbf{r}) \Delta w_{\kappa}^{(n-m)}(\mathbf{r}) d\mathbf{r} \quad (26)$$

The earlier implementation by Thompson *et al.*³⁰ used $\lambda \approx 0.1$ and $n_h = 0$ (referred to as simple mixing) until err_n dropped below a threshold of $\tau = 10^{-2}$, and then switched to $\lambda = 1$ and $n_h \approx 4$. Here we devise a more robust procedure, where λ , n_h and τ_n are adjusted dynamically as the iteration proceeds. We still apply simple mixing until $\text{err}_n \leq \tau_n$ and $n \geq 4$, and then switch to Anderson mixing, starting with $n_h = 3$ and increasing it after every iteration up to a maximum of $n_h = 30$.

The mixing parameter starts off at $\lambda = 0.2$ and is adjusted after every iteration (for both simple mixing and Anderson mixing) according to the change in err_n and the value of

$$\gamma = \frac{d_{01}}{d_{11}} = \cos(\alpha) \sqrt{\frac{\text{err}_n}{\text{err}_{n-1}}} \quad (27)$$

where α is an effective angle between the directions of $\Delta w_{\kappa}^{(n-1)}(\mathbf{r})$ and $\Delta w_{\kappa}^{(n)}(\mathbf{r})$. If $\text{err}_n > (1.1\text{err}_{n-1})$ or $\gamma < -0.5$, we deem the iterations to be proceeding poorly and therefore decrease λ to $\max(0.7\lambda, 0.1)$. If instead $\gamma > 0.5$, we assume the iterations are proceeding in the correct direction but too slowly and therefore increase λ to $\min(1.05\lambda, 1)$. Otherwise, we assume all is well and keep λ fixed.

The threshold at which Anderson mixing cuts in is initially set to $\tau_n = 10^{-2}$. After each simple mixing iteration, τ_n is increased to $\min(1.005\tau_n, 0.02)$ to ensure that Anderson mixing is eventually enabled. After each Anderson mixing iteration, we set τ_n to $\min(0.995\tau_n, 10\text{err}_n)$. Occasionally, the error in the next iteration, err_{n+1} , will exceed τ_n . If this happens, we decrease τ_n by the same factor of 10 and resume with simple mixing until err_n drops below τ_n .

2.4. Alignment

Convergence of the self-consistent field equations can be compromised by the fact that the solutions may drift due to their invariance with respect to additive constants and to arbitrary rotations about the

particle center. Setting the spatial average of the fields to zero prevents drift by additive constants. However, this still allows angular drift, which is sometimes the main source of difference between the input and output fields (*i.e.*, $\Delta w_{\kappa}(\mathbf{r})$). To cope with this, we modify the field eqn (1) and (2) by substituting $\phi_{\kappa}^{(n)}(\mathbf{r})$ by $\hat{\mathcal{R}}_n \phi_{\kappa}^{(n)}(\mathbf{r})$, where the rotation operator, $\hat{\mathcal{R}}_n$, is adjusted at each iteration such that

$$\hat{\mathcal{R}}_n \phi_{\kappa}^{(n)}(\mathbf{r}) \approx \phi_{\kappa}^{(n-1)}(\mathbf{r}) \quad (28)$$

so as to align the concentration with that of the previous iteration. The change in $\hat{\mathcal{R}}_n$ from one iteration to the next is generally very small, and so we update it by applying three successive rotations about the z , y and x axes,

$$\hat{\mathcal{R}}_n = \hat{\mathcal{R}}^x \hat{\mathcal{R}}^y \hat{\mathcal{R}}^z \hat{\mathcal{R}}_{n-1} \quad (29)$$

where $\hat{\mathcal{R}}_0$ is set to the identity operator.

To calculate the angle of the first rotation operator, $\hat{\mathcal{R}}^z$, we compare the spherical-harmonic expansions of $\hat{\mathcal{R}}_{n-1} \phi_{\kappa}^{(n)}(\mathbf{r})$ and $\phi_{\kappa}^{(n-1)}(\mathbf{r})$. By expressing the expansions⁴⁹ as

$$f(\mathbf{r}) = \sum_{\ell} \left\{ f_{\ell 0}(r) N_{\ell 0} P_{\ell 0}(\cos(\theta)) + \sum_{m>0} \tilde{f}_{\ell m}(r) \times N_{\ell m} P_{\ell m}(\cos(\theta)) \cos(m(\varphi - \varphi_{\ell m}^z(r))) \right\} \quad (30)$$

we obtain a distribution of phase factors, $\varphi_{\ell m}^z(r)$, about the z axis. The phase differences, $\Delta\varphi_{\ell m}^z(r)$, between $\hat{\mathcal{R}}_{n-1} \phi_{\kappa}^{(n)}(\mathbf{r})$ and $\phi_{\kappa}^{(n-1)}(\mathbf{r})$, are then reduced to a single value, $\overline{\Delta\varphi^z}$, by averaging over κ , r , ℓ and m . Since terms with larger coefficients should be more reliable, we weight the average by the mean value of $\tilde{f}_{\ell m}^2(r)$ from the expansions of $\hat{\mathcal{R}}_{n-1} \phi_{\kappa}^{(n)}(\mathbf{r})$ and $\phi_{\kappa}^{(n-1)}(\mathbf{r})$. We also disregard all angles greater than 0.06° from the distribution, which prevents erratic behavior from occurring before the fields have a chance to settle into a well-defined morphology.

The next rotation angle, $\overline{\Delta\varphi^y}$, is evaluated in the same way, except that we first rotate $\hat{\mathcal{R}}^z \hat{\mathcal{R}}_{n-1} \phi_{\kappa}^{(n)}(\mathbf{r})$ and $\phi_{\kappa}^{(n-1)}(\mathbf{r})$ by 90° so as to reorient their y directions along the z axis. The third angle, $\overline{\Delta\varphi^x}$, is obtained in an analogous fashion. All the rotations are performed using the SHTOOLS 2.5 software package.⁶³

3. Results

This section demonstrates our numerical algorithm on a diblock-copolymer film, with an intermediate segregation of $\chi N = 25$ and a thickness of $L = 0.5R_0$, grafted to a spherical core, with a radius of $R_c = R_0$. We first illustrate the efficiency of our iteration scheme for solving the self-consistent fields and then assess the effect of the finite mesh resolution, Δs , Δr , $\Delta\theta$ and $\Delta\varphi$. Once an adequate mesh resolution is determined, we predict the sequence of equilibrium morphologies as a function of diblock composition, f . The study finishes by investigating some of the peculiar packing effects resulting from the finite surface area of the particle core.

3.1. Iteration scheme

The first step of a SCFT study is to identify solutions for a comprehensive set of candidate morphologies. Some of ours have been obtained with the Drolet-Fredrickson approach⁶⁴ of starting from random fields, sometimes requiring 10,000 or more

iterations to reach a self-consistent solution. Others were obtained by, for example, scanning across f in increments of Δs , using the fields of the previous composition as the initial fields for the current composition. In this case, convergence is usually achieved in 40–200 iterations when there is no change in the symmetry of the morphology, and in 1000–4000 iterations when the system switches to a new morphology. Although the number of iterations can be large, the search for candidate morphologies is usually performed at a low mesh resolution where the cost per iteration is minimal.

Generally, the time consuming part of a SCFT study is tracing out the phase boundaries with respect to the system parameters (*i.e.*, χN , f , R_c and L), which typically has to be done at higher mesh resolutions. For these calculations, however, one starts from initial fields corresponding to the correct morphology, for which Anderson mixing performs admirably. Fig. 2 illustrates the convergence of the fields at $f = 0.31$ to an error of 10^{-6} , starting from a previous solution obtained at $f = 0.30$. In this particular case, convergence is achieved in just 51 iterations. To compare, simple mixing (*i.e.*, $n_h = 0$) takes 145 iterations when using an adaptive mixing parameter and 333 iterations for a fixed $\lambda = 0.2$.

3.2. Resolution tests

Here we investigate the quantitative effect the mesh resolution (*i.e.*, n_s , n_r , n_θ and n_ϕ) has on our results. So that the maximum angular separation in ϕ approximately matches that in θ , we set $n_\phi = 2(n_\theta - 1)$.²⁵ Our experience also suggests that it is best to match the angular and radial widths of ΔV , which for our ratio of L/R_c is approximately achieved by setting $n_\theta = 5n_r$.

Fig. 3 illustrates how well the algorithm conserves material by plotting $|V^{-1} \int (\phi_A(\mathbf{r}) + \phi_B(\mathbf{r})) d\mathbf{r} - 1|$. The deviation from perfect conservation falls rapidly as the spatial mesh becomes finer, but it is nearly independent of the mesh spacing along the chain contour, which is why it is only plotted for $n_s = 201$. Our modified Crank–Nicolson method was devised so as to achieve this high level of conservation. However, the concentration of individual segments, $\phi(\mathbf{r}, s) = q(\mathbf{r}, s)q^i(\mathbf{r}, s)$, is not conserved nearly so well, as illustrated in Fig. 3 for the junction point, $s = f$.

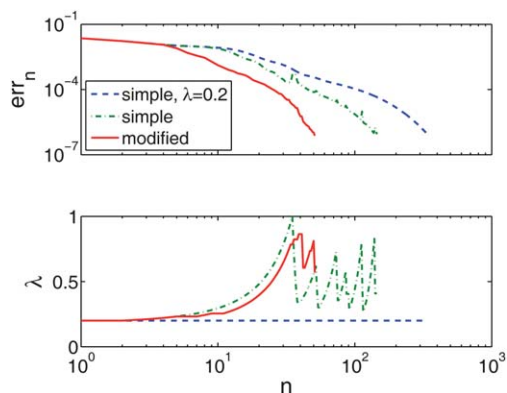


Fig. 2 Performance of our modified iteration scheme (solid curves) for solving the fields equations compared to that of simple mixing with (dash-dotted curve) and without (dashed curve) an adaptive mixing parameter, λ . The reduction in err_n and the variation in λ are plotted as a function of the number of iterations, n .

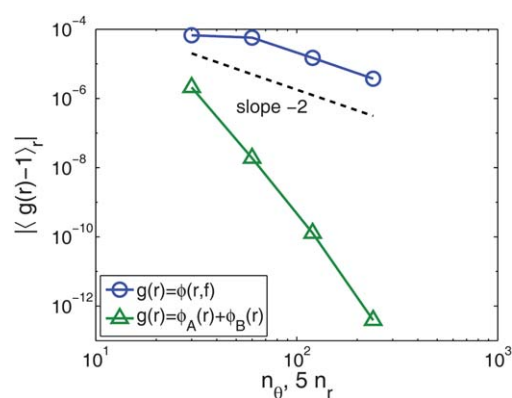


Fig. 3 Conservation of polymer material (triangles) and of junction points (circles) with increasing spatial resolution at a fixed number, $n_s = 201$, of grid points along the chain contour.

Because of this, the conservation of total material is significantly degraded if we deviate from the simple trapezoid method for integrating $\phi(\mathbf{r}, s)$ over $s = 0$ to 1.⁵⁹

The rotational drift between subsequent iterations of the fields, as specified by the rotation operator $\hat{\mathcal{R}}_n$, represents a violation of the self-consistent conditions, eqn (1) and (2). Fig. 4 examines the total angle corresponding to $\hat{\mathcal{R}}_n$ for converged solutions of a spiral morphology. Reassuringly, the rotational drift vanishes as the mesh resolution increases.

Naturally, the rotational invariance in the self-consistent field solutions will be somewhat violated by the anisotropy of the real-space mesh, but this should vanish as the mesh resolution increases. Fig. 5 demonstrates this by comparing the free energy difference, ΔF , between two solutions of the same stripe morphology rotated 90° with respect to each other. As expected, $\Delta F \rightarrow 0$ as the spatial resolution increases. At first glance, the smaller value of $n_s = 101$ seems to produce the more accurate result, but this is just a case of the numerical error being accidentally small for this particular rotation angle. Indeed, the error for $n_s = 101$ becomes large when the angular separation is changed to 15° . Of course, ΔF should remain small for all possible rotations.

In reality, the required level of accuracy depends on which quantity one wishes to calculate. Since our primary interest is the position of phase boundaries, Fig. 6 examines the influence of the mesh resolution on the transition between two stripe phases. We

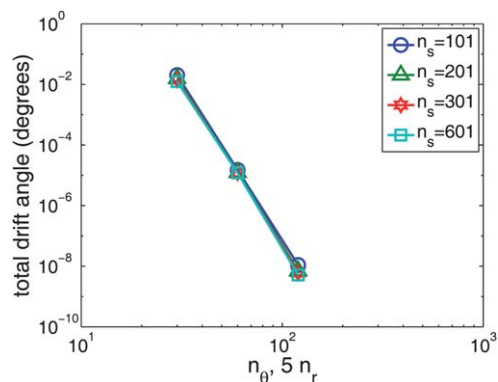


Fig. 4 Angular drift of the fields per iteration (defined by the rotational operator, $\hat{\mathcal{R}}_n$) plotted as a function of the mesh resolution.

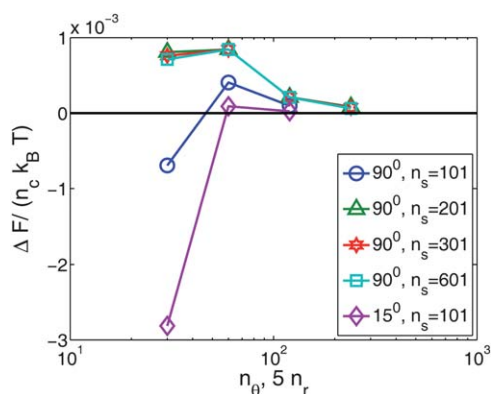


Fig. 5 Difference in free energy, ΔF , between two orientations of the same stripe morphology plotted as a function of mesh resolution.

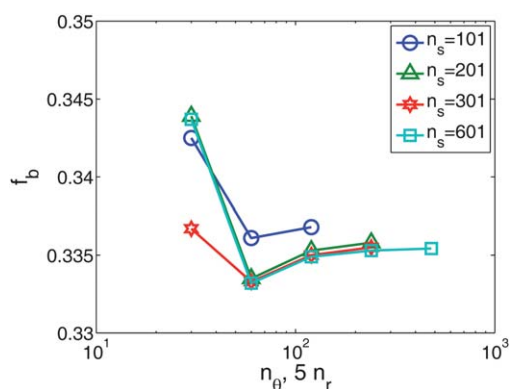


Fig. 6 Convergence of a metastable phase boundary, f_b , between two stripe phases plotted as a function of mesh resolution.

choose morphologies with rotational symmetry in ϕ so as to consider higher values of n_s and $n_\theta = 5n_r$. On the basis of the results, $n_s = 201$ and $n_\theta = 5n_r = 60$ are sufficient to locate the phase boundaries to within $\Delta f \approx 0.005$. Thus these values are used for our subsequent calculations, apart from a few cases where we double the spatial resolution to confirm our numerical accuracy.

3.3. Stability of the morphologies

The free energies, F , of the candidate morphologies are plotted in Fig. 7 as a function of composition, f . Apart from the uniform phase, where the morphology has no angular dependence, the free energy differences are too small on this scale to identify the curves of lowest energy representing the stable equilibrium phases. Therefore, we fit the locus of free energy minima to a fifth-order polynomial, $F_0(f)$,⁶⁵ to obtain a smooth function that closely tracks the general trend in the free energy. Then by plotting the small differences, $F - F_0(f)$, the curves corresponding to the equilibrium phases and the boundaries where they cross can be readily identified.

The resulting boundaries and equilibrium phases are displayed in Fig. 8. The morphologies are visualized by coloring the A-rich domains red, while omitting the B-rich domains; the inner and outer surfaces of the film (*i.e.*, $r = R_c$ and $r = R_c + L$) are shown transparently with dark and light blue, respectively. The phases

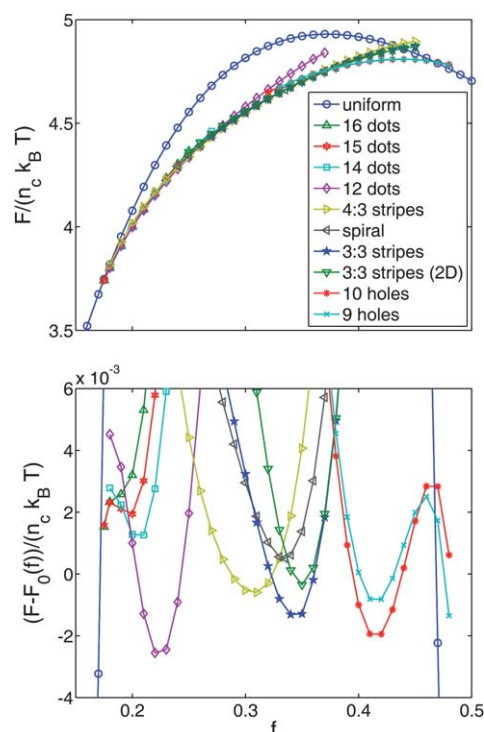


Fig. 7 Free energies, F , of the competing morphologies as a function of diblock composition, f , plotted on an absolute scale (top) and relative to a fifth-order polynomial fit, $F_0(f)$, to the equilibrium free energy (bottom).

come in three distinct flavors, which we classify as dots, stripes and holes, according to the topology of their A-rich domains. The different dot and hole morphologies are labeled by the number of dots and holes, respectively, while the stripe morphologies are labeled with two integers referring to the number of distinct A- and B-rich surface domains.

The phase transitions for the spherical brush are shifted significantly relative to those of the flat brush calculated earlier.⁴ Part of the reason is the curved geometry in which the area of the film expands as $(R_c + z)^2$, where z refers to the distance from the substrate. Following this rationale, we map the flat-brush profiles, $\phi_A^{\text{flat}}(\mathbf{r})$, onto an effective composition for the spherical brush using

$$f_{\text{eff}} = \frac{4\pi}{VA_{\text{cell}}} \int_{\text{cell}} \phi_A^{\text{flat}}(\mathbf{r})(R_c + z)^2 d\mathbf{r} \quad (31)$$

where A_{cell} is the area of one unit cell of the flat brush. With this, one can transform a phase boundary from the flat brush system to that of the curved geometry. Of course, the two phases at the boundary will give slightly different values of f_{eff} , but the difference is small and so we just take the average value. Fig. 9 shows that this simple mapping does indeed account for the general shift in the phase boundaries.

The numerical sequence of dots, stripes and holes that occurs with increasing f is readily explained by the previous flat-brush calculation,⁴ which found that domain size expands as f increases. Since the total area, A , of the nanoparticle is fixed, the number of dots, stripes and holes must then decrease with increasing f . Indeed, this is exactly what is observed in Fig. 8.

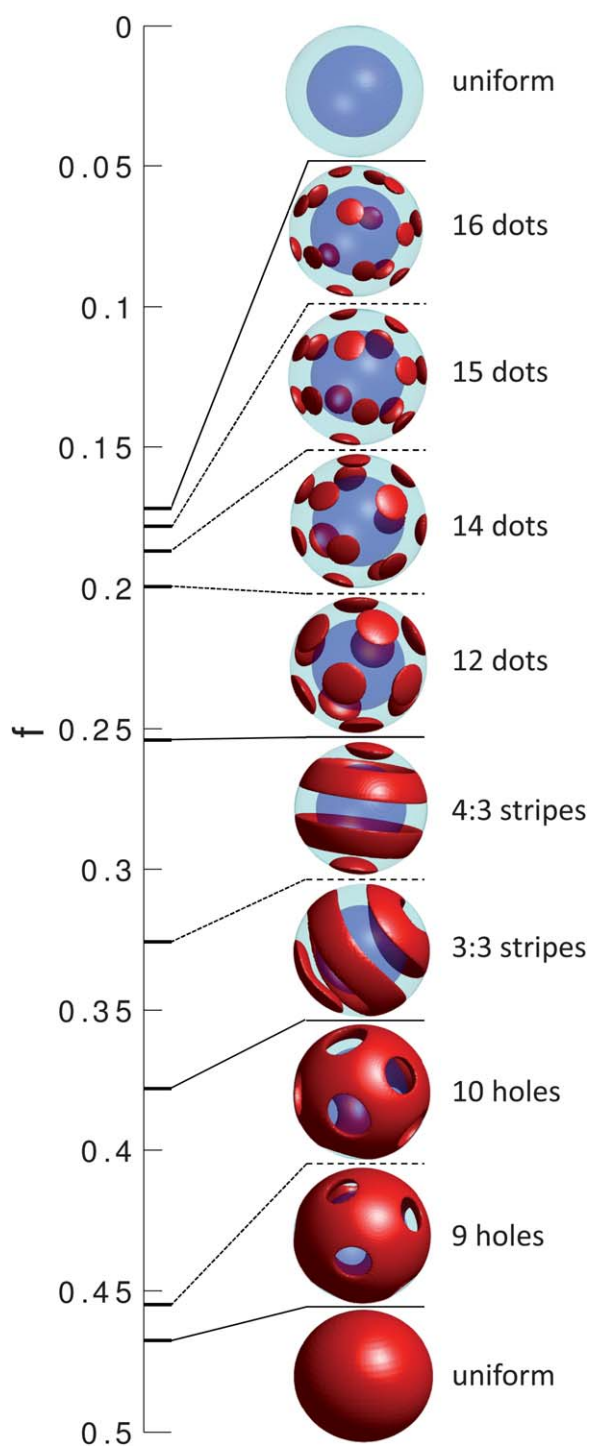


Fig. 8 Stable morphologies and their regions of stability for $\chi N = 25$, $L = 0.5R_0$ and $R_c = R_0$. The A-rich domains are shown in red and the B-rich domains are omitted.

Our calculations generated a considerable number of metastable morphologies, some of which are depicted in Fig. 10. They are often a mixture of stripes with dots or holes (e.g., Fig. 10a or 10b), and as such are nearly stable around the stripe/dot or stripe/hole phase boundary, respectively. Similarly, the phase with a single hole (Fig. 10c) is almost stable at the hole/uniform boundary. There are also various defective stripe phases (e.g.,

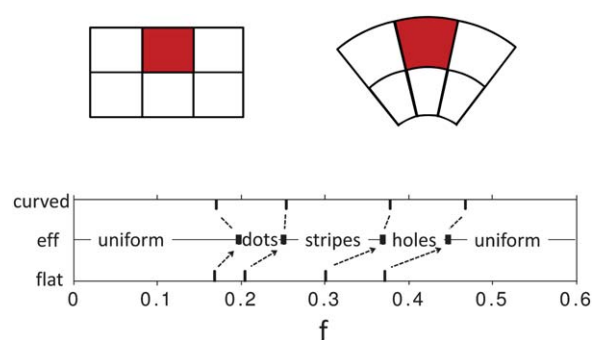


Fig. 9 Shift in the phase boundaries due to deforming the morphologies of a flat brush (upper left) into those of a spherical brush (upper right). The plot illustrates how the boundaries of the flat brush⁴ (lower ticks) approximately map onto those of the spherical brush in Fig. 8 (upper ticks) using f_{eff} defined in eqn (31).

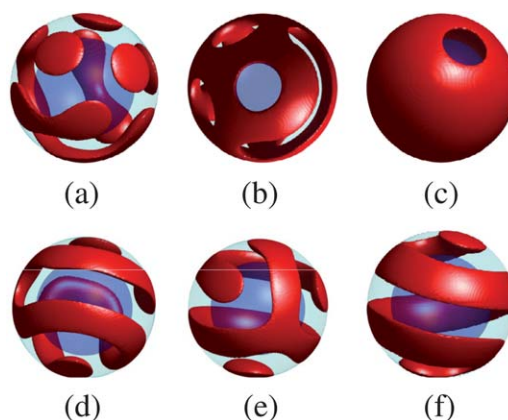


Fig. 10 Examples of metastable morphologies with free energies slightly above those of the stable morphologies in Fig. 8.

Fig. 10d and 10e) that compete for stability in the stripe region. A few metastable phases, such as the spiral phase in Fig. 10f, are defect free and could become stable under suitable conditions. Indeed, the 2D SCFT calculations of Chantawansri *et al.*²⁵ for non-grafted films obtained a spiral phase, which was metastable at small R_c but became stable at larger R_c .

3.4. Packing frustration

It may seem surprising that the 13-dot morphology is omitted in the sequence of stable phases (Fig. 8), but this also happened in the 2D study of Chantawansri *et al.*²⁵ This is because it has to compete with the exceptional stability of the 12-dot phase, which

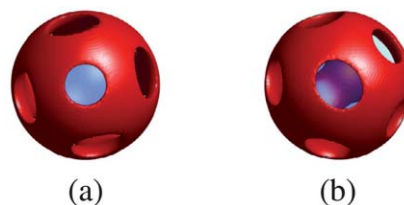


Fig. 11 Two orientations of the 10-hole morphology illustrating the difference between holes with (a) 4 neighbors and (b) 5 neighbors.

occupies an abnormally large region of the phase diagram. This is linked to the fact that 12 dots can arrange at the vertices of a perfect icosahedron, where each dot has five evenly distributed neighbors of equal distance producing a relatively isotropic environment in which it can nearly acquire an ideal circular shape. As a result of having circular shapes of identical size, the stretching of the individual molecules is well balanced, which helps maintain a lower free energy.^{43,66} In most cases, however, the packing of the dots (or holes) is far less ideal, as illustrated in Fig. 11 for the 10-hole phase. Performing a Voronoi construction, we find that two of the holes have four neighbors (Fig. 11a) while the other eight holes have five neighbors (Fig. 11b). The former two are small and circular, while the latter eight are elliptical and 33% larger. This variation in size and deviation from circular is indicative of packing frustration, which reduces the stability of the phase.

Likewise, the stripe phases show interesting effects due to packing frustration. We start by considering the rotationally-symmetric (*i.e.*, 2D) 4:3-stripe morphology in Fig. 8, where the A-rich domains form two rings near the equator and a dot at each pole. The tendency of the A-rich domains to expand as f increases⁴ is partially constrained by the finite area of the sphere. This restriction on the lateral area of the A-rich domains pushes them deeper into the film, particularly for the dots, as illustrated in Fig. 12.

At sufficiently large f , one of the dots finally disappears transforming the 4:3-stripe morphology into a 3:3-stripe morphology with a dot at one pole and a hole at the other pole. As a result of eliminating one domain, the dot and hole swell to such an extent that their circular shape becomes unstable (Fig. 7). Consequently, they switch to an oblong shape with their major axes oriented in perpendicular directions, breaking the rotational symmetry in ϕ (Fig. 13a). As f increases further, the stripes widen allowing the dot and hole to shrink, which in turn reduces their aspect ratio until they eventually become circular (Fig. 13b). The point at which the aspect ratio reaches one corresponds to a second-order symmetry-breaking transition.

4. Discussion

One of the merits of our new algorithm is its computational speed. The CPU time to complete one iteration of the field equations is a mere 8 seconds on a single core of a 2.6 GHz AMD Opteron processor for $n_s = 201$, $n_r = 12$, $n_\theta = 60$ and $n_\phi = 118$. Even for runs from random initial fields requiring thousands of

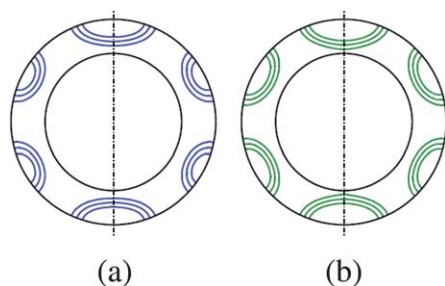


Fig. 12 Contours of constant concentration, $\phi_A(\mathbf{r}) = 0.25, 0.50$ and 0.75 , plotted in vertical slices through the 4:3-stripe morphology (dashed lines denote the z axis) at its phase boundaries, (a) $f = 0.254$ and (b) $f = 0.326$.

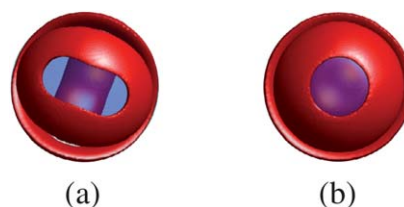


Fig. 13 Polar view of the 3:3-stripe morphology at its phase boundaries, (a) $f = 0.326$ and (b) $f = 0.378$.

iterations, the total time required to obtain a self-consistent solution is generally on the order of hours. When we start from a good initial guess corresponding to the correct morphology, the time is reduced to minutes. Since the time required to solve the diffusion equation scales as $n_s n_r \ell_{\max}^3 \ln(\ell_{\max})$,²⁵ the calculation will remain feasible for considerably larger particles. This performance can be contrasted with the real-space algorithm devised by Roan,²⁷ for which self-consistent solutions for a similar system involving mixed brushes can take years of CPU time. Although Roan²⁷ provided insufficient details to make an accurate comparison, it appears that the present algorithm is orders of magnitude faster.

There is certainly some opportunity for improving our algorithm. For instance, the modified Crank–Nicolson step only solves eqn (14) approximately. We could improve the accuracy by performing multiple Crank–Nicolson steps per Δs interval, but this immediately reduces the degree to which material is conserved (Fig. 3) just as when we deviate from integrating with the trapezoid method. Another possibility is to use a forth-order pseudo-spectral scheme,⁶⁷ although initial attempts⁵⁶ have not worked well, perhaps because of the delta function in eqn (8) for $q^i(\mathbf{r}, 1)$. In any case, if one was to do this they should also replace the Crank–Nicolson step and the trapezoid integration by higher-order schemes. As for solving the self-consistent field conditions, we cannot imagine doing much better than 40–200 iterations, as is the case when we have a good initial guess for the fields. However, there may be better ways of generating candidate structures, such as using a simpler phenomenological model.^{20,21} Furthermore, the calculation time might be reduced, particularly for larger particles, by using alternative algorithms for the spherical-harmonic transformations that scale as $\ell_{\max}^2 \ln(\ell_{\max})$.⁶⁸ Of course, a substantial reduction in real time could be achieved by parallelizing the code.

An advantage of the microscopic approach of SCFT is that it can be readily applied to other systems or modified to include additional effects that might be necessary for quantitative comparison with experiment. For instance, we could have just as easily modeled binary homopolymer brushes, or in fact any combination of chain types, grafted or not. Modifications could include a surface affinity for one of the polymer components with the air,⁴ or the ability of the polymer film to adjust the topography of its outer surface.²³ Rather than fixing the grafting density, we could permit the grafting points to slide freely over the surface of the core.⁶⁹ The SCFT can also treat solvated conditions as easily as melt conditions. Furthermore, the algorithm is not just limited to films on the surface of a sphere; it could equally well handle polymers confined to a spherical cavity.^{36,70}

SCFT does have a certain number of limitations owing to the fact that it is a mean-field theory. For instance, the polymer density should be reasonably high so that there is significant overlap between chains, or otherwise the mean-fields will not provide an accurate representation of the environment. The spheres should also contain a sufficient number of chains (e.g., $n_c > 10^3$), or otherwise the phase transitions predicted by SCFT will be smeared out by thermal fluctuations. For there to be abrupt transitions, the differences in free energy between structures should vary rapidly on the scale of $k_B T$ with respect to the system parameters (e.g., f).

Researchers are likely to be more interested in the equilibrium morphologies (Fig. 8) than the defect-type patterns of the metastable morphologies (Fig. 10). Our calculations find that the energy gap between them is often quite small, and so we could expect metastable morphologies to readily occur, which is evidently the case in both experiment^{12,13} and simulation.¹⁸ Thus the segregation and particle size should not become too large, or else the thermal fluctuations will be insufficient to overcome the energy barriers⁷¹ that tend to trap the particles in metastable morphologies.

The interesting frustration effects resulting from the finite surface area of the sphere are similar to those encountered in block-copolymer melts confined to cylindrical or spherical cavities. They are also reminiscent of packing effects in other non-polymeric systems. Take, for instance, the Tammes problem⁴⁰ where a given number of circular disks are arranged on the sphere so as to maximize the minimum separation. This is very similar to our arrangement of dots (or holes), because the packing frustration is reduced by making the space between the dots (or holes) as uniform in thickness as possible.⁶⁶ However, our polymeric problem has additional degrees of freedom in that the dots (or holes) can exchange area and their shape can deviate from circular, albeit at some energetic cost. There is also the Thomson problem⁴¹ of finding the minimum energy of placing a certain number of electrons on a sphere. Interestingly, the arrangement of block-copolymer micelles has been previously approximated by electrostatic interactions.⁷⁴ Although our polymeric problem is distinct from the Tammes and Thomson problems, there are a number of commonalities, such as the *magic* numbers of 6 and 12, where packing is nearly ideal and

likewise the tendency of the packing to be particularly frustrated for certain other numbers, such as 8 and 11 (Table 1).

5. Summary

This article introduces an efficient algorithm for solving the SCFT for structured polymers in a three-dimensional spherical geometry. The polymer concentrations are obtained by solving the diffusion equations with the pseudo-spectral method for the angular coordinates²⁵ and a modified Crank–Nicolson method for the radial direction. The self-consistent field conditions are adjusted iteratively using Anderson mixing with adaptive parameters and a rotational-alignment technique. The total calculation time of the algorithm appears to be orders of magnitude faster than the real-space algorithm developed earlier by Roan.²⁷

The algorithm could be readily applied to a wide range of spherical systems, such as mixed brushes grafted to spherical nanoparticles or diblock-copolymer melts in spherical cavities. Here it is demonstrated on a thin diblock-copolymer film of thickness $L = 0.5R_0$ tethered to a spherical core of radius $R_c = R_0$ (Fig. 1). The equilibrium sequence of self-assembled morphologies is predicted as a function of diblock composition, f , at fixed segregation, $\chi N = 25$ (Fig. 8). The sequence follows the general trend predicted for flat substrates,⁴⁴ where the end-block domains transform from dots to stripes to a layer with holes and finally to a uniform shell. There are also a large number of non-equilibrium morphologies (Fig. 10) containing defects of sufficiently low energy that they would likely appear in experiments.

Particularly interesting is how the detailed behavior is affected by the constraint of a finite surface area. For instance, the 3:3-stripe phase undergoes a symmetry-breaking transition (Fig. 13), when there is a poor match between the width of its stripes and the circumference of the particle. Likewise, the dot and hole morphologies experience significant degrees of frustration, which results in a distribution of sizes and shapes with a variance that depends on the number of dots or holes (Fig. 11). For *magic* numbers such as 12, the variance vanishes, resulting in an increased stability, reminiscent of what happens in the Tammes problem^{39,40} of positioning disks on a spherical surface or the Thomson problem^{39,41} of placing charged particles on a sphere.

Added note

On the basis of further details provided by Roan while this paper was in press, our algorithm is approximately two orders of magnitude faster than the real-space algorithm in Ref. 27. One of the orders can be attributed to our pseudo-spectral method for solving the diffusion equation, while the other is due to the faster convergence of our scheme for solving the field equations.

Acknowledgements

We are grateful to Ian Hamley, Ben O'Driscoll and An-Chang Shi for useful discussions. This work was supported by grants from the EPSRC (EP/F029616/1 and EP/G026203/1), the NSF (DMR-0904499) and the NRF (2009-0089230 and 2010-0005949).

Table 1 Equilibrium properties of the Thomson problem for n_{obj} electrons on a sphere, specifying the number n_i of electrons with i neighbors (as defined by a Voronoi construction), the number n_{dist} of distinct neighbor distances, the average angular separation $\langle \Theta \rangle$, and the standard deviation σ_Θ of the separation.^{72, 73}

n_{obj}	n_4, n_5, n_6	n_{dist}	$\langle \Theta \rangle$	σ_Θ
6	6, 0, 0	1	90.0°	0°
7	5, 2, 0	2	84.0°	8.49°
8	4, 4, 0	3	83.1°	14.90°
9	3, 6, 0	3	74.0°	6.96°
10	2, 8, 0	3	70.3°	6.65°
11	2, 8, 1	9	67.0°	7.15°
12	0, 12, 0	1	63.4°	0°
13	1, 10, 2	13	61.5°	5.74°
14	0, 12, 2	3	59.1°	4.42°
15	0, 12, 3	7	57.2°	5.18°
16	0, 12, 4	4	55.3°	4.49°
17	0, 12, 5	4	54.3°	6.61°

Notes and references

- 1 R. A. Segalman, *Mater. Sci. Eng., R*, 2005, **48**, 191–226.
- 2 B. Akgun, G. Ugur, W. J. Brittain, C. F. Majkrzak, X. F. Li, J. Wang, H. M. Li, D. T. Wu, Q. Wang and M. D. Foster, *Macromolecules*, 2009, **42**, 8411–8422.
- 3 B. M. D. O'Driscoll, G. H. Griffiths, M. W. Matsen, S. Perrier, V. Ladmiral and I. W. Hamley, *Macromolecules*, 2010, **43**, 8177–8184.
- 4 M. Matsen and G. Griffiths, *Eur. Phys. J. E*, 2009, **29**, 219–227.
- 5 J. F. Marko and T. A. Witten, *Phys. Rev. Lett.*, 1991, **66**, 1541–1544.
- 6 D. Usov, V. Gruzdev, M. Nitschke, M. Stamm, I. Luzinov, I. Tokarev and S. Minko, *Macromolecules*, 2007, **40**, 8774–8783.
- 7 J. Wang and M. Müller, *J. Phys. Chem. B*, 2009, **113**, 11384–11402.
- 8 M. Müller, *Phys. Rev. E*, 2002, **65**, 030802.
- 9 M. Motornov, Y. Roiter, I. Tokarev and S. Minko, *Prog. Polym. Sci.*, 2010, **35**, 174–211.
- 10 B. Zhao and L. Zhu, *Macromolecules*, 2009, **42**, 9369–9383.
- 11 D. Li, X. Sheng and B. Zhao, *J. Am. Chem. Soc.*, 2005, **127**, 6248.
- 12 B. Zhao and L. Zhu, *J. Am. Chem. Soc.*, 2006, **128**, 4574–4575.
- 13 L. Zhu and B. Zhao, *J. Phys. Chem. B*, 2008, **112**, 11529–11536.
- 14 X. Jiang, G. Zhong, J. M. Horton, N. Jin, L. Zhu and B. Zhao, *Macromolecules*, 2010, **43**, 5387–5395.
- 15 X. Jiang, B. Zhao, G. Zhong, J. M. Horton, L. Zhu, R. S. Hafner and T. P. Lodge, *Macromolecules*, 2010, **43**, 8209.
- 16 R. P. Carney, G. A. DeVries, C. Dubois, H. Kim, J. Y. Kim, C. Singh, P. K. Ghorai, J. B. Tracy, R. L. Stiles, R. W. Murray, S. C. Glotzer and F. Stellacci, *J. Am. Chem. Soc.*, 2008, **130**, 798–799.
- 17 B. M. D. O'Driscoll and I. W. Hamley, (work in progress).
- 18 C. Singh, P. K. Ghorai, M. A. Horsch, A. M. Jackson, R. G. Larson, F. Stellacci and S. C. Glotzer, *Phys. Rev. Lett.*, 2007, **99**, 226106.
- 19 A. Seifpour, P. Spicer, N. Nair and A. Jayaraman, *J. Chem. Phys.*, 2010, **132**, 164901.
- 20 P. Tang, F. Qiu, H. Zhang and Y. Yang, *Phys. Rev. E*, 2005, **72**, 016710.
- 21 M. Pinna, X. Guo and A. V. Zvelindovsky, *Polymer*, 2008, **49**, 2797–2800.
- 22 D. Meng and Q. Wang, *J. Chem. Phys.*, 2009, **130**, 134904.
- 23 J. U. Kim and M. W. Matsen, *Phys. Rev. Lett.*, 2009, **102**, 078303.
- 24 J. F. Li, J. Fan, H. D. Zhang, F. Qiu, P. Tang and Y. L. Yang, *Eur. Phys. J. E*, 2006, **20**, 449–457.
- 25 T. L. Chantawansri, A. W. Bosse, A. Hexemer, H. D. Ceniceros, C. J. García-Cervera, E. J. Kramer and G. H. Fredrickson, *Phys. Rev. E*, 2007, **75**, 031802.
- 26 S. V. Lishchuk, *J. Phys. A: Math. Theor.*, 2009, **42**, 465401.
- 27 J.-R. Roan, *Phys. Rev. Lett.*, 2006, **96**, 248301.
- 28 J.-R. Roan, *Int. J. Mod. Phys. B*, 2004, **18**, 2469–2475.
- 29 K. Ø. Rasmussen and G. Kalosakas, *J. Polym. Sci.: Part B*, 2002, **40**, 1777–1783.
- 30 R. B. Thompson, K. Ø. Rasmussen and T. Lookman, *J. Chem. Phys.*, 2004, **120**, 31–34.
- 31 B. Yu, P. Sun, T. Chen, Q. Jin, D. Ding, B. Li and A.-C. Shi, *J. Chem. Phys.*, 2007, **127**, 114906.
- 32 W. Li and R. A. Wickham, *Macromolecules*, 2009, **42**, 7530–7536.
- 33 M. Ma, V. Krikorian, J. H. Yu, E. L. Thomas and G. C. Rutledge, *Nano Lett.*, 2006, **6**, 2969–2972.
- 34 H. Q. Xiang, K. Shin, T. Kim, S. Moon, T. J. McCarthy and T. P. Russell, *J. Polym. Sci.: Part B*, 2005, **43**, 3377–3383.
- 35 Y. Y. Wu, G. S. Cheng, K. Kasov, S. W. Sides, J. F. Wang, T. J., G. H. Fredrickson, M. Moskovits and C. D. Stucky, *Nat. Mater.*, 2004, **3**, 816–822.
- 36 T. Higuchi, A. Tajima, K. Motoyoshi, H. Yabu and M. Shimomura, *Angew. Chem., Int. Ed.*, 2008, **47**, 8044–8046.
- 37 T. Higuchi, A. Tajima, K. Motoyoshi, H. Yabu and M. Shimomura, *Soft Matter*, 2008, **4**, 1302–1305.
- 38 B. Yu, B. H. Li, Q. H. Jin, D. Ding and A.-C. Shi, *Macromolecules*, 2007, **40**, 9133–9142.
- 39 T. Aste and D. Weaire, *The pursuit of perfect packing*, Institute of Physics Publishing, Ltd, Bristol, UK, 2000.
- 40 R. Tammes, *Rec. Trav. Bot. Neerl.*, 1930, **27**, 1–84.
- 41 J. J. Thomson, *Philos. Mag.*, 1904, **7**, 237–265.
- 42 G. H. Fredrickson, *The equilibrium theory of inhomogeneous polymers*, Oxford University Press, New York, USA, 2006.
- 43 M. W. Matsen, *J. Phys.: Condens. Matter*, 2002, **14**, R21–R47.
- 44 M. W. Matsen, in *Soft Matter, Vol. 1: Polymer Melts and Mixtures*, edited by G. Gompper and M. Schick, Wiley-VCH, Weinheim, 2006.
- 45 M. Matsen, *Macromolecules*, 2010, **43**, 1671–1674.
- 46 J.-R. Roan, *Phys. Rev. Lett.*, 2001, **87**, 059902.
- 47 M. Tuckerman, B. J. Berne and G. J. Martyna, *J. Chem. Phys.*, 1992, **97**, 1990–2001.
- 48 At the edge of the mesh, the cells are defined by $r = R_c$ to $R_c + \Delta r/2$ for $i = 0$, $r = R_c + L - \Delta r/2$ to $R_c + L$ for $i = n_r - 1$, $\theta = 0$ to $\Delta\theta/2$ for $j = 0$, and $\theta = \pi - \Delta\theta/2$ to π for $j = n_\theta - 1$.
- 49 The spherical harmonics are defined as $Y_{lm}(\theta, \varphi) = N_{lm} P_{lm}(\cos(\theta)) \cos(m\varphi)$ for $m \geq 0$ and $Y_{lm}(\theta, \varphi) = N_{lm} P_{lm}(\cos(\theta)) \sin(|m|\varphi)$ for $m < 0$, where $P_{lm}(u)$ are associated Legendre polynomials and N_{lm} are normalization constants such that $\int Y_{lm}^2 d\Omega = 1$.
- 50 Available at <http://www.scd.ucar.edu/css/software/spherepack>.
- 51 J. C. Adams and P. N. Swarztrauber, *Mon. Weather Rev.*, 1999, **127**, 1872–1878.
- 52 A. R. Mitchell and D. F. Griffiths, *The Finite Difference Method in Partial Differential Equations*, John Wiley & Sons Ltd, Chichester, UK, 1980.
- 53 H. F. Trotter, *Proc. Am. Math. Soc.*, 1959, **10**, 545–551.
- 54 R. L. Leveque, *Finite volume methods for hyperbolic problems*, Cornell University Press, New York, USA, 2002.
- 55 G. Strang, *SIAM J. Numer. Anal.*, 1968, **5**, 506–517.
- 56 T. L. Chantawansri, Ph.D. Thesis, University of California, Santa Barbara (2009).
- 57 W. Press, S. Teukolsky, W. Vetterling and B. Flannery, *Numerical Recipes in Fortran: the art of scientific computing*, Cornell University Press, Cambridge, UK, 2nd edn, 1992.
- 58 R. D. Smith, *Numerical solution of partial differential equations: finite difference methods*, Oxford University Press, Oxford, UK, 1993.
- 59 M. W. Matsen, *J. Chem. Phys.*, 2004, **121**, 1938–1948.
- 60 R. L. Burden and D. J. Faires, *Numerical Analysis*, Brooks Cole, sixth edn, 1997.
- 61 J. M. Ortega and W. C. Rheinboldt, *Iterative Solution of Nonlinear Equations in Several Variables*, Academic Press, New York, USA, 1970.
- 62 F. Schmid, *Phys. Rev. E*, 1997, **55**, 5774–5784.
- 63 Available at <http://www.ipgp.fr/~wieczor/SHTOOLS/SHTOOLS.html>.
- 64 F. Drolet and G. H. Fredrickson, *Phys. Rev. Lett.*, 1999, **83**, 4317–4320.
- 65 $F_0(f)/(n_c k_B T) = -4.336 + 108.599 f - 574.503 f^2 + 1596.792 f^3 - 2233.226 f^4 + 1228.921 f^5$.
- 66 M. W. Matsen and F. S. Bates, *Macromolecules*, 1996, **29**, 7641.
- 67 E. Cochran, C. Garcia-Cervera and G. Fredrickson, *Macromolecules*, 2006, **39**, 2449.
- 68 R. Suda and M. Takami, *Math. Comput.*, 2002, **71**, 703–715.
- 69 J. U. Kim and M. W. Matsen, *Soft Matter*, 2009, **5**, 2889–2895.
- 70 J. J. Cerda, T. Sintes and R. Toral, *J. Chem. Phys.*, 2009, **131**, 134901.
- 71 X. Cheng, L. Lin, W. E., P. Zhang and A.-C. Shi, *Phys. Rev. Lett.*, 2010, **104**, 148301.
- 72 T. Erber and G. M. Hockney, *J. Phys. A: Math. Gen.*, 1991, **24**, L1369–L1377.
- 73 Results in Table 1 are calculated using the electron positions quoted by K. S. Brown, <http://www.mathpages.com/HOME/kmath005/kmath005.htm>.
- 74 A. N. Semenov, *Sov. Phys. JETP*, 1985, **61**, 733–742.